This is a repository copy of *Efficient photoredox co-upcycling of CO2 and plastic waste by band-gap-engineered ZnxCd1–xS catalyst*.

White Rose Research Online URL for this paper:
https://eprints.whiterose.ac.uk/222308/

Version: Accepted Version

Efficient Photoredox Co-Upcycling of CO_2 and Plastic Waste by Band-Gap Engineered $Zn_xCd_{1-x}S$ Catalyst

Yi Zhang,[1] Ming-Yu Qi,[2] Marco Conte,[3] Zi-Rong Tang,*[1,4] and Yi-Jun Xu*[1,2]

[1] College of Chemistry, State Key Laboratory of Photocatalysis on Energy and Environment, Fuzhou University, Fuzhou 350116, P. R. China

[2] Institute of Fundamental and Frontier Sciences, University of Electronic Science and Technology of China, Chengdu 611731, P. R. China

[3] School of Mathematical and Physical Sciences, University of Sheffield, Sheffield, S3 7HF, UK

[4] School of Materials and Energy, University of Electronic Science and Technology of China, Chengdu 611731, P. R. China

ABSTRACT

Solar-driven CO_2 reduction combined with plastic waste valorization presents a versatile approach to simultaneously reset misaligned hydrocarbon resources and achieve a carbon-neutral cycle. Herein, we demonstrate a co-upcycling heterogeneous photoredox catalysis for efficient CO_2 reduction to tunable syngas, integrated with polyethylene terephthalate (PET) plastic conversion for accessing acetate, over the spherical band-gap engineered $Zn_xCd_{1-x}S$ catalyst. The key to steering the syngas H_2/CO rate is to modulate the conduction band bottom potentials of the $Zn_xCd_{1-x}S$ photocatalysts by altering the Zn/Cd ratio, which results in syngas H_2/CO production in a wide range. Moreover, controlled variations in the molar ratio of Zn/Cd regulate the electron-hole separation capability, thereby endowing $Zn_{0.8}Cd_{0.2}S$ with the optimum syngas and acetate production rates. The underlying mechanistic origin of such a redox reaction involving CO_2-assisted PET plastic conversion is systematically investigated. This win-win cooperative photoredox catalysis offers a tantalizing possibility for co-upcycling CO_2 and PET into value-added feedstocks.

TOC GRAPHIC
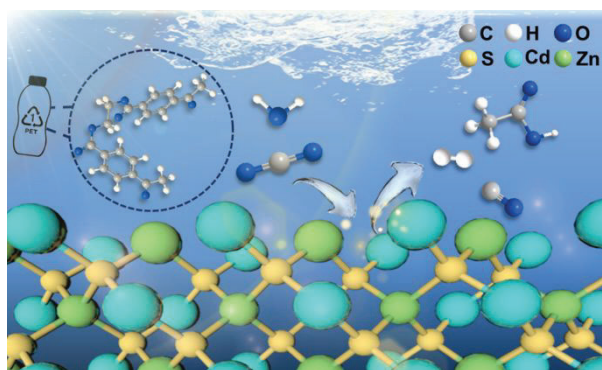
2

Upcycling greenhouse gases like CO_2 into green and sustainable products driven by solar energy is an appealing approach for simultaneously alleviating the environmental energy crisis and tackling carbon neutrality by capturing CO_2.[1-5] Of the various CO_2 reduction products, CO is the two-electron reduction product, and thus a kinetically more viable option compared to CH_4 and CH_3OH, which require eight and six proton-electron transfers, respectively, to form a molecule.[6-10] More importantly, CO, a key C_1 feedstock, plays an irreplaceable role in the industrial processes in the form of syngas intermediate, a mixture of H_2 and CO, such as gasification of coal and Fischer–Tropsch synthesis.[11,12] Solar-driven CO_2 reduction with H_2O, known as artificial photosynthesis, wonderfully mimics the masterpiece of nature and admirably achieves renewable and clean syngas production.[1,13-15] However, this real overall reaction is always inefficient or difficult due to the sluggish half-reaction kinetics of O_2.[11,13] Alternatively, diverse sacrificial reagents (e.g., ascorbic acid, triethanolamine, and methanol) are employed to consume holes to achieve the overall reaction, which undoubtedly results in a waste of oxidation capacity and increases the system cost.[16-18] In this regard, photocatalytic plastic waste valorization, with a dehydrogenation process to reset misaligned hydrocarbon resources, can be deftly combined with CO_2 reduction to constitute a redox cycle, blazing a fascinating trail for the simultaneous co-upcycling of greenhouse gas and plastic waste into beneficial chemicals, like killing two birds with one stone.[19-22]

Very recently, the prominent valorization of plastic waste while producing valuable products has become extremely appealing due to the aggravation of "white pollution" and the shortage of resources.[23-25] These mushrooming demonstrations of photocatalytic plastic conversion mainly focus on CdS-based catalysts.[26-28] However, the photogenerated holes in the relatively negative valence band position of CdS are insufficient for completely and efficiently oxidizing the plastics.[13,29,30] Besides, the intrinsic photocorrosion behavior of CdS also significantly constrains its stability for practical applications.[20] Therefore, the rational development of a preferable photocatalyst with sufficient oxidation capability and good stability is of crucial importance for photocatalytic upcycling of plastic waste. Notably, $Zn_xCd_{1-x}S$ ($0 \leq x \leq 1$) formed by the introduction of Zn to CdS, possessing these aforementioned characteristics, has been considered a highly promising platform for improving this redox reaction system.[20] Variations in the molar ratio of Zn/Cd not only modulate the band structure, but also facilitate the electron-hole separation,[19,31-33] which could be used as a feasible strategy for cooperatively tuning CO_2 reduction combined with plastic waste valorization in one photoredox cycle.

In this study, we first report the cooperative co-upcycling of CO_2 and polyethylene terephthalate (PET) plastic into tunable syngas and acetate in one photoredox reaction system by designing spherical $Zn_xCd_{1-x}S$ photocatalysts with different Zn/Cd molar ratios. The syngas H_2/CO ratio is well regulated over a wide range, including a ratio of 3:2, which is a desirable composition for alkane synthesis. Mechanistic studies have unambiguously revealed that $Zn_xCd_{1-x}S$ can efficiently adsorb CO_2 molecules, thus facilitating CO_2 photoreduction along the $CO_2 \rightarrow *CO_2 \rightarrow *COOH \rightarrow *CO \rightarrow CO$ reaction pathways. Simultaneously, the cooperation of the energetic holes and •OH promotes the conversion of PET to acetate. In addition, the successful and efficient conversion of post-consumer PET plastic concomitantly with CO_2 reduction has revealed the tantalizing possibility of artificial sunlight-driven systems in actual manufacturing industries.

The $Zn_xCd_{1-x}S$ nanospheres with different Zn/Cd molar ratios (x = 0, 0.2, 0.4, 0.5, 0.6, 0.8, and 1) have been synthesized following the schematic illustration described in **Figure S1**. For this synthesis, a facile hydrothermal process with zinc acetate [$Zn(CH_3COO)_2 \cdot 2H_2O$], cadmium acetate [$Cd(CH_3COO)_2 \cdot 2H_2O$], and thiourea ($NH_2CSNH_2$) as precursors is used.[31] The transmission electron microscopy (TEM) and scanning electron microscopy (SEM) obviously show the morphologies and microscopic structures of $Zn_{0.8}Cd_{0.2}S$. As shown in **Figures 1a** and **S2**, the as-synthesized $Zn_{0.8}Cd_{0.2}S$ shows a uniform spherical shape with an average diameter of 173.5 ± 6.7 nm. High-resolution TEM (HRTEM) image reveals the distinct lattice fringe (**Figure 1b**), where the interlayer distance of 0.315 nm is indexed to the (111) lattice plane. The (111) lattice spacing of $Zn_{0.8}Cd_{0.2}S$ is significantly lower than $Zn_{0.6}Cd_{0.4}S$ (0.34 nm), and this is attributed to Vegard's law, as the molar ratio of Zn increases, the lattice distance of $Zn_xCd_{1-x}S$ gradually decreases, thus indicating a homogeneous structure.[19,31,34] As manifested in **Figure S3**, energy-dispersive X-ray spectroscopy (EDX) analysis further indicates the existence of S, Cd, and Zn elements. The results of high-angle annular dark field scanning-TEM (HAADF-STEM) and elemental mapping reconfirm the successful synthesis of $Zn_xCd_{1-x}S$ photocatalyst (**Figure 1c**).

X-ray photoelectron spectroscopy (XPS) has been performed in order to carefully determine the valence states and chemical element compositions. The survey spectrum of $Zn_{0.8}Cd_{0.2}S$ demonstrates the coexistence of Zn, Cd, and S (**Figure S4**), which is further corroborated by EDX data. For CdS and ZnS samples, the characteristic peaks of Cd 3d located at 411.1 eV (Cd 3$d_{3/2}$) and 404.3 eV (Cd 3$d_{5/2}$) are monitored to Cd^{2+} valence state (**Figure 1d**), while the Zn 2$p_{1/2}$ and 2$p_{3/2}$ binding energies (1044.7 eV and 1021.6 eV) are ascribed to the Zn^{2+} (**Figure 1e**).[35,36] For $Zn_{0.8}Cd_{0.2}S$ sample, the S 2p spectrum is deconvoluted into two peaks at 163.1 eV and 161.6 eV, with peak positions between those of CdS and ZnS (**Figure 1f**). The peak positions of Cd 3d show a 0.4 eV shift towards higher values, and those of Zn 2p shift to lower values by 0.1 eV, in comparison to that of CdS and ZnS samples, respectively. This is due to the charge redistribution between Zn and Cd atoms in the $Zn_{0.8}Cd_{0.2}S$ sample.[37] Moreover, to gain the crystal phase information of $Zn_xCd_{1-x}S$, X-ray diffraction (XRD) measurements have been performed (**Figure 1g**).[32] As the Zn to Cd atomic ratio increases, because the radius of Zn^{2+} (0.74 Å) is smaller than that Cd^{2+} (0.97 Å),[38,39] a diffraction peak shift to higher scattering angles is observed, further confirming the synthesis of $Zn_xCd_{1-x}S$ rather than composites or physical mixtures of CdS and ZnS. As illustrated in **Figure 1h**, the UV/Vis diffuse reflectance spectrum (DRS) shows that the light absorption edge of $Zn_xCd_{1-x}S$ appears redshifted as the proportion of Cd increases. Subsequently, we have calculated the band gap energy of $Zn_xCd_{1-x}S$ based on DRS spectroscopy combined with the Kubelka-Munk method (**Figure S5**);[40] meanwhile, the conduction band (CB) has been measured by the Mott-Schottky curves, finally obtaining the energy band structural image (**Figures 1i** and **S6**).[41] The results reveal that both the valence band (VB) and CB positions become positive with increasing Zn concentration, indicating that the band structure of $Zn_xCd_{1-x}S$ is modulated flexibly.
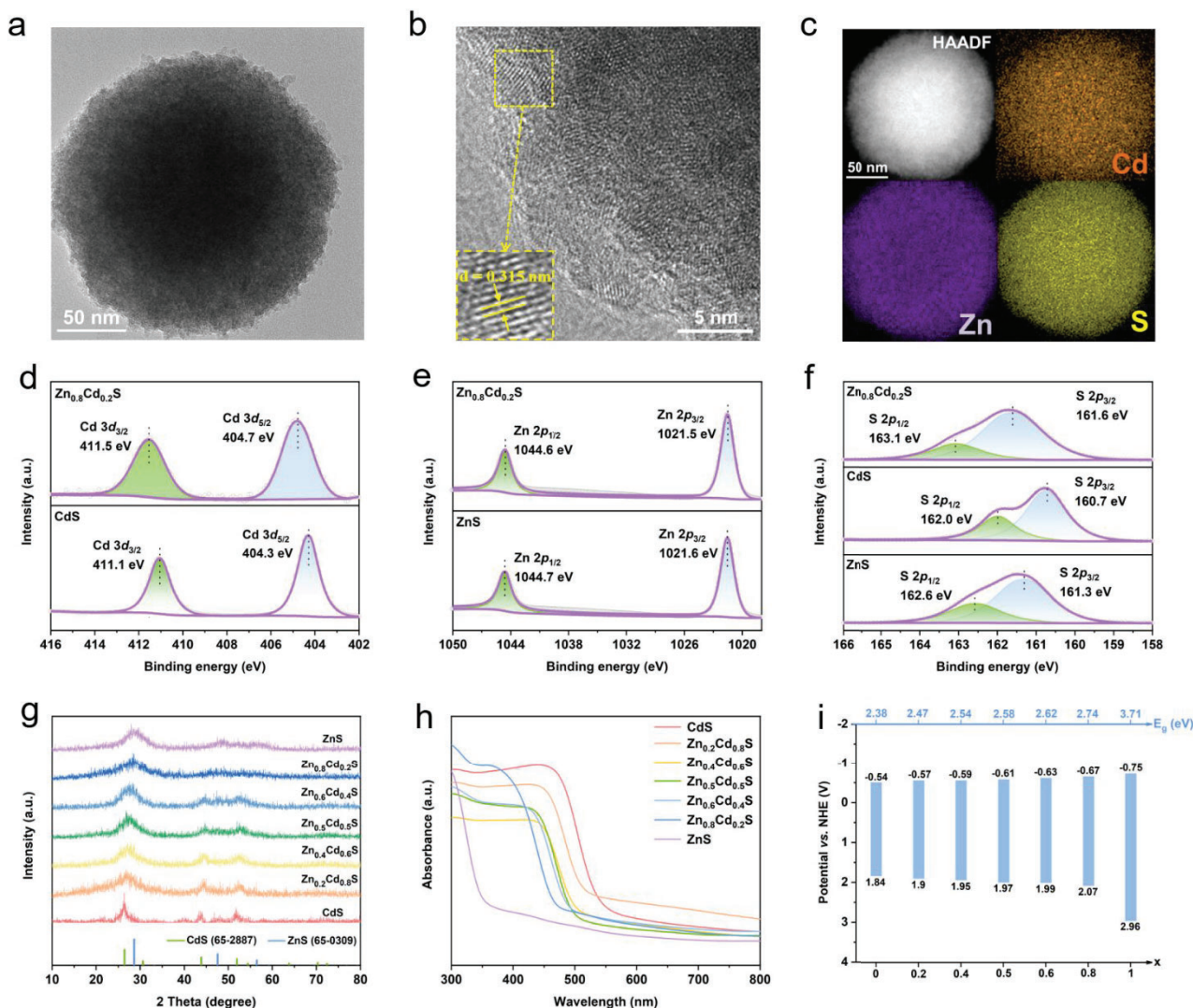
Figure 1. (a) TEM image, (b) HRTEM image, and (c) HAADF-STEM and the element mapping results of $Zn_{0.8}Cd_{0.2}S$. XPS spectra of the samples: (d) Cd $3d$ of $Zn_{0.8}Cd_{0.2}S$ and CdS; (e) Zn $2p$ of $Zn_{0.8}Cd_{0.2}S$ and ZnS; (f) S $2p$ of $Zn_{0.8}Cd_{0.2}S$, CdS, and ZnS. (g) XRD patterns, (h) DRS spectroscopy, and (i) CB and VB potentials of $Zn_xCd_{1-x}S$. The VB potential of $Zn_xCd_{1-x}S$ is calculated based on the equation $E_{VB} = E_{CB} + E_g$.

The photocatalytic assay of CO_2 and polyethylene terephthalate (PET) co-upcycling (**Figure 2a**) in a photoredox system has been carried out under CO_2 atmosphere and Xe-lamp irradiation (**Figure S7**). Initially, taking ethylene glycol (EG) as a model substrate, the optimal reaction conditions have been explored, owing to a large proportion of EG in PET released during alkaline solution pretreatment.[42] As shown in **Figure S8**, $Zn_{0.8}Cd_{0.2}S$ exhibits the highest activity. Subsequently, the optimum alkaline reaction condition based on $Zn_{0.8}Cd_{0.2}S$ has been investigated (**Figure S9**). The resulting syngas production gradually decreases with increasing potassium hydroxide (KOH) concentration, and all of the following experimental pretreatment reaction solutions are diluted to 1 mol L^{-1}, taking into account the need for PET pretreatment under harsh alkaline conditions and the need to reduce the corrosiveness and cost of the system.
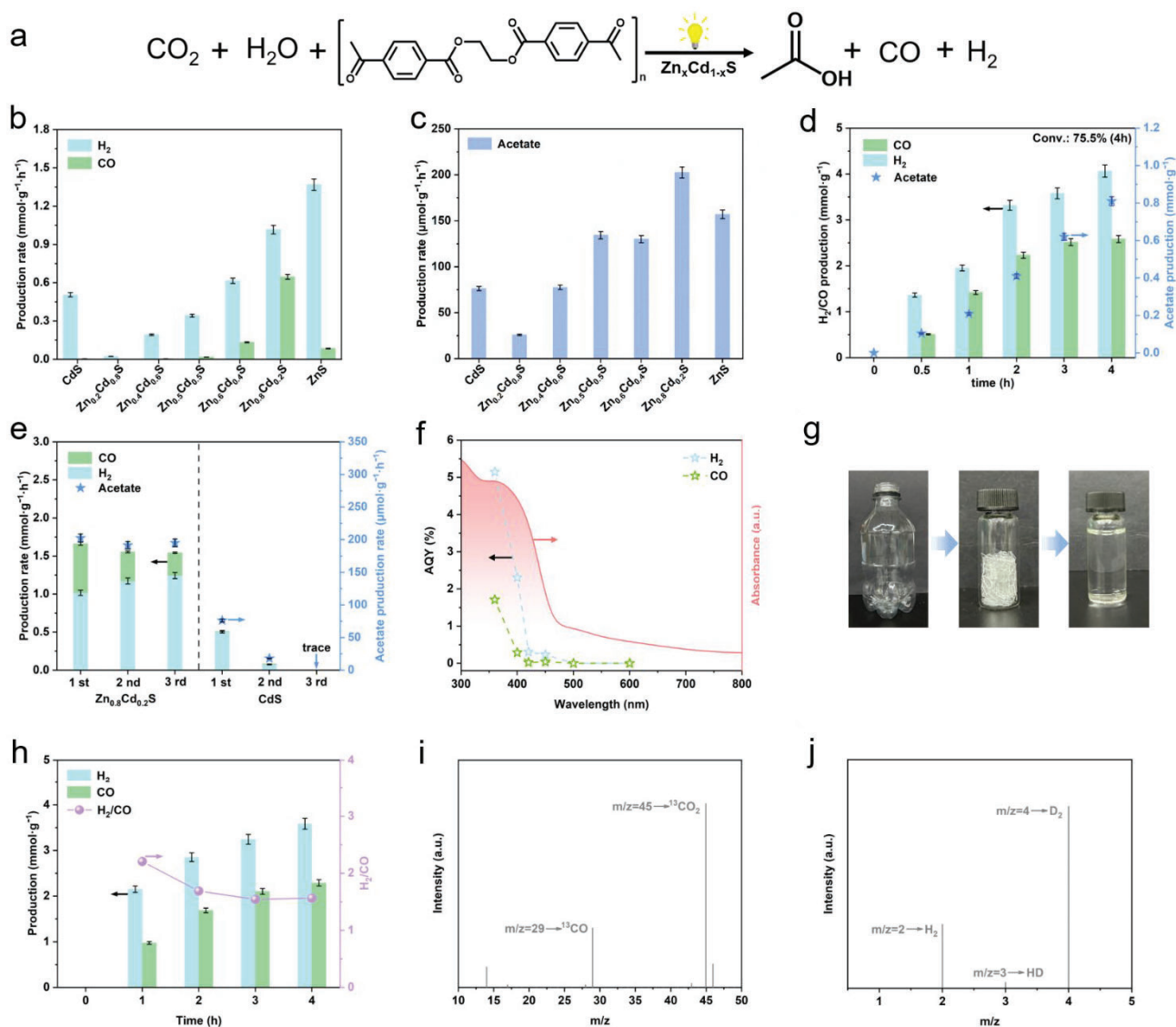
Figure 2. (a) Scheme for co-upcycling of CO_2 and PET plastic. (b) CO/H_2 production rate during photocatalytic conversion of PET over $Zn_xCd_{1-x}S$. (c) Acetate production rate during photocatalytic conversion of PET over $Zn_xCd_{1-x}S$. (d) Time-yield plots over $Zn_{0.8}Cd_{0.2}S$. (e) Recycling performance of $Zn_{0.8}Cd_{0.2}S$ and CdS. (f) DRS spectrum of $Zn_{0.8}Cd_{0.2}S$ and AQYs for CO/H_2 production over $Zn_{0.8}Cd_{0.2}S$ under different monochromatic lights. (g) Pretreatment of used PET bottles. (h) The performance test of CO_2 reduction paired with used PET bottles conversion over $Zn_{0.8}Cd_{0.2}S$. (i) Mass spectrum of ^{13}CO (m/z = 29) and (j) D_2 (m/z = 4) produced over $Zn_{0.8}Cd_{0.2}S$ in the photocatalytic reduction. Reaction conditions: 10 mg catalysts, 10 mL reaction liquid, full spectrum, irradiation for 4 h.

A series of commercial PET photoactivity tests have been performed under the same conditions with the variation of Zn ratio (**Figures 2b** and **2c**). Commercial PET plastics are pretreated with an alkali solution, and standard samples in the same alkali solution are calibrated to identify the detected substance (**Figures S10-S11**). As confirmed by ^1H nuclear magnetic resonance (NMR) spectroscopy, EG and terephthalate (TPA) in PET are released. The significant variability in the amount of EG before and after light illumination, and little variation in the amount of TPA (**Figures S12-S13**),

6

suggests that the liquid phase product is derived from the oxidation of EG rather than TPA. Similar to the model reaction, $Zn_{0.8}Cd_{0.2}S$ still maintains the optimal photocatalytic performance, displaying that the highest production rate of syngas and acetate is 1.7 mmol·g^{-1}·h^{-1} and 202.5 μmol·g^{-1}·h^{-1}, respectively; moreover, the resulting syngas H_2/CO ratio is well regulated over a wide range, including a ratio of 3:2, which is a desirable composition for alkane synthesis (**Figure S14**).[43,44] The $Zn_{0.8}Cd_{0.2}S$ sample exhibits excellent syngas and acetate yields compared to other representative catalysts (**Table S1**). ^{13}C NMR spectroscopy and ion chromatography detecting CO_3^{2-} concentration in reaction solution before and after light illumination have indicated that PET is also substantially converted into CO_3^{2-} during the reaction (**Figures S15** and **S16**). The time profiles in **Figure 2d** show that the production of acetate and H_2/CO increases along with time during the reaction, and the conversion rate of PET reaches 75.5% after 4 h of irradiation. In order to evaluate the stability of $Zn_{0.8}Cd_{0.2}S$, the cycle experiments have been implemented. As depicted in **Figure 2e**, the production rate of acetate and H_2/CO remains stable during long repeated trials, with the slight change in performance, which could be attributed mainly to the partial loss of the catalyst. The used $Zn_{0.8}Cd_{0.2}S$ still shows a uniform spherical shape (**Figure S17**). A comparison of the XRD patterns and XPS spectra of the fresh and used $Zn_{0.8}Cd_{0.2}S$ is shown in **Figure S18**, where no significant deviations are observed, which also suggests the excellent stability of the samples. In distinct contrast, CdS exhibits poor stability, with an 84% reduction in H_2/CO production in the second cycle and a gradual loss of activity in the third cycle. As displayed in **Table S2**, the Cd^{2+} leaching results from the inductively coupled plasma optical emission spectrometer (ICP-OES) also demonstrate that the introduction of Zn inhibits the photocorrosion and improves the recovery of samples from the reaction solvent. In addition, the cyclic stability of ZnS is slightly worse than that $Zn_{0.8}Cd_{0.2}S$ (**Figure S19**). The apparent quantum yields (AQYs) of this reaction are closely associated with the incident light wavelength while matching well with the UV/Vis DRS result of $Zn_{0.8}Cd_{0.2}S$ (**Figure 2f**). Evidently, the syngas has achieved an optimal AQY of 6.85% at λ = 350 nm, even exceeding the single CO_2 reduction of most reported sacrificial reaction systems (**Table S3**).[11,17] Encouraged by the potential results above, we have transformed to estimate the catalytic performance of post-consumer PET plastic bottle conversion integrated with syngas production. The bottles are cut into pieces (**Figure 2g**) and pretreated under the same condition (**Figures S20** and **S21**). As expected, this reaction delivers efficient conversion over $Zn_{0.8}Cd_{0.2}S$, with the syngas H_2/CO ratio stabilizing at 3:2 after 3 h of reaction, and the total production of syngas at 4 h reaches 5.9 mmol·g^{-1}, which closes to that of commercial PET photocatalytic activity at the same reaction time (6.6 mmol·g^{-1}) (**Figure 2h**). Besides, the acetate production is 220 μmol·g^{-1}, and these results confirm the potential practical application of $Zn_{0.8}Cd_{0.2}S$ for co-upcycling of CO_2 and post-consumer PET plastic waste into value-added chemicals.

To demonstrate the redox synergy of CO_2 reduction and PET plastic valorization, and to explore the origin of CO and H_2, a series of trace and contrast experiments have been carried out. The isotopic labeling tests directly trace the carbon and hydrogen sources, and validate that the CO product arises from the photoreduction of externally purged CO_2 gas and the generated H_2 mainly originates from H_2O instead of PET constituent monomers, where the spectral signals at m/z = 29 and m/z = 4 are attributed to [13]CO and D_2, respectively. (**Figures 2i** and **2j**). The reaction in pure Argon (Ar) indicates that only trace amounts of CO (0.9 μmol) are observed, proving that CO from the PET overoxidation is negligible (**Figure S22**).[45,46] Subsequently, the solutions containing PET

are further substituted with H_2O, and the comparison reaction of CO_2 reduction with H_2O oxidation has been carried out (**Figure S23**). Due to the sluggish kinetics of O_2 evolution, the syngas H_2/CO production is significantly reduced when H_2O becomes the proton source. This result confirms that the introduction of PET consumes holes to produce acetate, thus overcoming the sluggish kinetics of O_2 evolution in the CO_2 conversion process and improving syngas production.

In order to clarify the underlying reaction mechanism of CO_2 reduction in combination with PET conversion, we have performed a wide range of control experiments under a variety of conditions, as disclosed in **Figure 3a**. The removal of light or catalyst contributes to the disruption of the reaction (entry 1 in **Figure 3a**), indicating that this is a $Zn_xCd_{1-x}S$ induced photoredox process. The introduction of the electron scavenger CCl_4 significantly constrains the H_2/CO production (entry 2 in **Figure 3a**), suggesting that photogenerated electrons play an integral part in the syngas production. Acetate production is reduced by 61% after the addition of the hole scavenger Na_2S (entry 3 in **Figure 3a**), unambiguously revealing the crucial role of photoexcited holes in the selective production of acetate by PET. Generally, benzoquinone (BQ) can be used as $\bullet O_2^-$ scavenger, and the production of acetate does not change significantly after BQ adding this reaction system, which indicates the absence of $\bullet O_2^-$ (entry 4 in **Figure 3a**).[47] Subsequently, to explore the role of $\bullet OH$ in the PET conversion process, methanol (ML) as $\bullet OH$ scavenger is added to the reaction system, and the electron paramagnetic resonance (EPR) test with 5,5-dimethyl-1-pyrrolin-N-oxide (DMPO) as a $\bullet OH$ trapping agent is carried out. As depicted in entry 5 in **Figure 3a**, the acetate production is decreased by only 24%. Significantly, no EPR characteristic signal peak of CdS, ZnS and $Zn_{0.8}Cd_{0.2}S$ is observed in the dark, and obvious $\bullet OH$ signals of $Zn_{0.8}Cd_{0.2}S$ are detected under full spectrum irradiation (**Figures 3b** and **S24**).[19] These above results have validated that $\bullet OH$ is also involved in the PET conversion process, but photogenerated holes dominate the activity and selectivity in the process.

The above photoactivity test information has demonstrated the tunability of syngas H_2/CO enabled by tuning the Zn ratio from 0 to 1. To gain insight into the origin of the changes in syngas production, the CO_2/CO TPD analyses of the as-prepared samples have been carried out. As shown in **Figures 3c** and **S25**, the peaks of CO_2 desorption on the catalysts can be approximately separated into three regions (50 °C - 180 °C, 180 °C - 350 °C and > 350 °C), corresponding to weak, moderate, and strong CO_2 adsorption sites, respectively.[48,49] No significant peak in CO_2 adsorption is observed in the CdS sample. Evidently, the CO_2 adsorption capacity for $Zn_{0.8}Cd_{0.2}S$ in medium and strong parts (180 °C - 550 °C) is lower than that of ZnS. On the other hand, $Zn_{0.8}Cd_{0.2}S$ also possesses a weaker CO adsorption capacity compared to those for ZnS (**Figure 3d**), indicating that the formed CO is easier to desorption on the surface of $Zn_{0.8}Cd_{0.2}S$. Besides, transient photocurrent responses and electrochemical impedance spectroscopy (EIS) have been conducted in order to explore the dynamic behaviors of charge separation and transportation. As disclosed in **Figures 3e** and **3f**, the $Zn_{0.8}Cd_{0.2}S$ sample has a faster charge carrier separation rate and lower charge transfer resistance than CdS and ZnS.[50,51] Moreover, the dynamic behaviors of charge separation and transportation have been explored by the time-resolved photoluminescence (TRPL) spectra (**Figure S26**). As shown in **Table S4**, the average lifetime of $Zn_{0.8}Cd_{0.2}S$ (τ_a = 3.13 ns) is shorter than that of CdS (τ_a = 3.98 ns) and ZnS (τ_a = 3.57 ns). The shortening of the decay lifetime confirms that $Zn_{0.8}Cd_{0.2}S$ has a more rapid interfacial charge transfer. Upon gathering the above results, we can draw the conclusion

that variations in the molar ratio of Zn/Cd not only modulate the band structure and charge carrier separation capability, improving the photoredox-catalyzed performance, but also regulate CO_2/CO adsorption, tuning the syngas CO/H_2 ratio over a wide range.
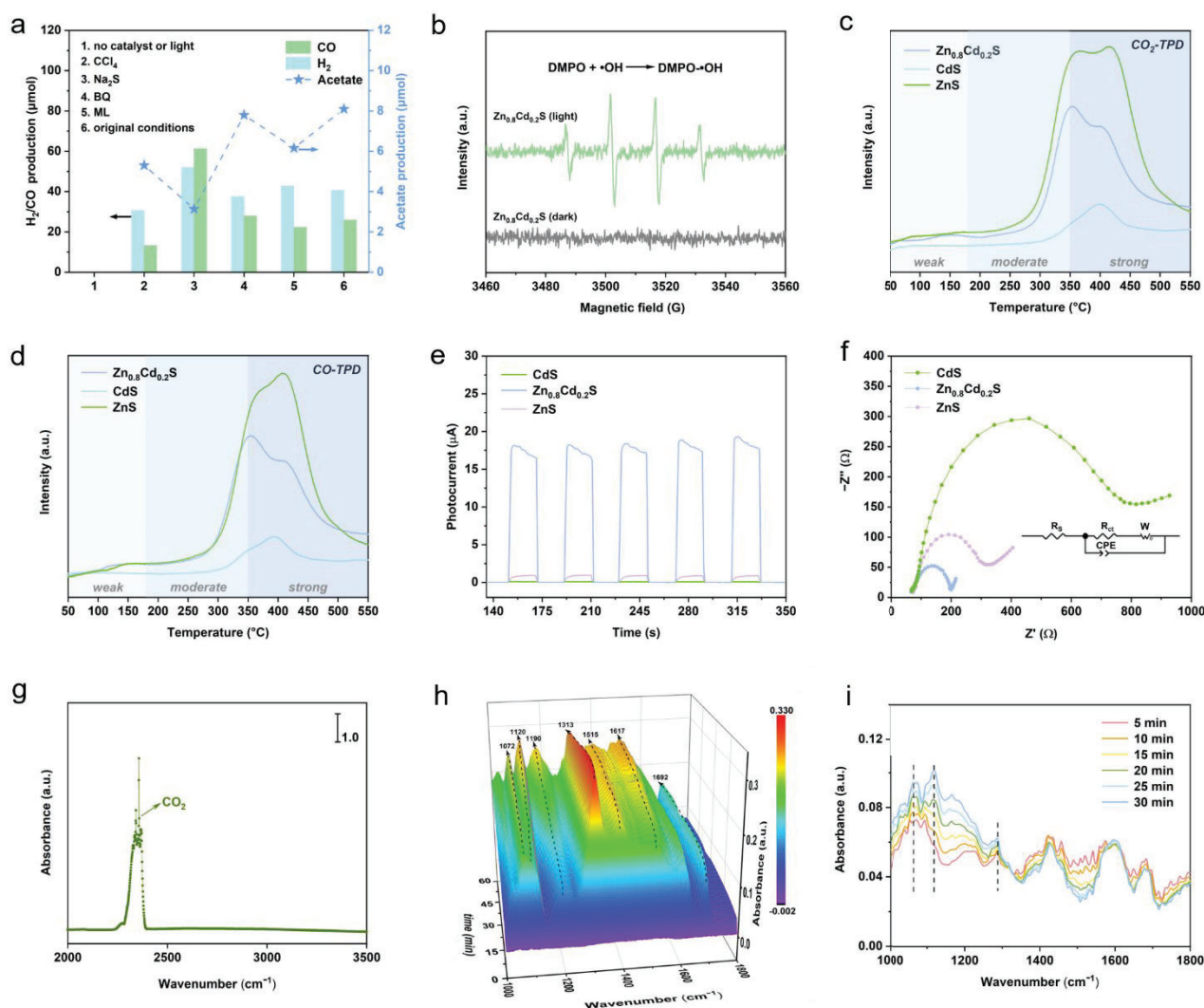

Figure 3. (a) Controlled tests over $Zn_{0.8}Cd_{0.2}S$ under various reaction conditions. (b) EPR spectra of $Zn_{0.8}Cd_{0.2}S$ using DMPO as the trapping agents (dark and light). (c) CO_2-TPD and (d) CO-TPD analyses over $Zn_{0.8}Cd_{0.2}S$, CdS, and ZnS. (e) Transient photocurrent responses of $Zn_{0.8}Cd_{0.2}S$, CdS, and ZnS. (f) EIS Nyquist plots of $Zn_{0.8}Cd_{0.2}S$, CdS, and ZnS. (g) In situ FT-IR spectroscopy of CO_2 adsorption. Time-resolved in situ FTIR spectra of (h) the photocatalytic CO_2 reduction paired with PET conversion and (i) PET conversion in Ar atmosphere over $Zn_{0.8}Cd_{0.2}S$.

In situ Fourier transform infrared spectroscopy (FT-IR) analysis has been evaluated to trace the reaction intermediates and dynamical transformation of the surface-adsorbed species during this co-upcycling cooperative reaction. CO_2 molecules adsorption over the $Zn_{0.8}Cd_{0.2}S$ surface has been first employed by successively purging with CO_2 for 20 min in the dark, and the emergence of IR characteristic CO_2 adsorption peaks in the 2250 - 2400 cm^{-1} range has indicated that CO_2 molecules are readily adsorbed on the surface of $Zn_{0.8}Cd_{0.2}S$ (**Figure 3g**).[52,53] Upon light irradiation, CO_2 reduction intermediates, including CO_2^- (1190 and 1692 cm^{-1}), *COOH (1515 and 1617 cm^{-1}), and

9

*HCOOH (1313 cm^{-1}), are obviously detected (**Figure 3h**).[54,55] The continuous increase of intermediates peak intensity over a period of 60 min strongly supports the CO_2 reaction pathway: $CO_2 \rightarrow {}^*CO_2 \rightarrow {}^*COOH \rightarrow {}^*CO \rightarrow CO$. In particular, the other two FT-IR signals at 1072 and 1120 cm^{-1} may arise from the primary alcohol in the PET conversion process.[47] To eliminate the effect of CO_2 intermediates and confirm the PET conversion process, the FT-IR analysis is performed again with Ar gas. As disclosed in **Figure 3i**, both peaks can still be clearly observed, and the ever-increasing strength of the peaks is a good indication that PET produces the intermediates of primary alcohol. Surprisingly, a peak of increasing intensity around 1300 cm^{-1} can still be observed, which is attributed to the production of vinyl alcohol.[56] Subsequently, the vinyl alcohol is converted to acetaldehyde because of the existence of keto-enol tautomerism.[57] Acetaldehyde is oxidized to acetate, and then under the alkaline condition part of the acetate is further decarboxylated to form CO_3^{2-}, which has been confirmed by the simulated experiment of acetate oxidation (**Figure S27**).[58]

Based on the aforementioned discussion, a logical and plausible mechanism for the co-upcycling of CO_2 and PET into syngas and acetate catalyzed by $Zn_xCd_{1-x}S$ has been proposed (**Figure 4**). Under optical irradiation, $Zn_xCd_{1-x}S$ absorbs the incident light and then the photoexcited electrons in the VB migrate to its CB, while holes are reserved in the VB and part of them oxidize H_2O to •OH. The pretreated PET is first oxidized by holes and •OH into vinyl alcohol through the primary alcohol. Subsequently, the resulting vinyl alcohol is converted to acetaldehyde, followed by the oxidation of acetaldehyde to acetate. Part of the acetate is desorbed from the surface of photocatalyst, and the remaining acetate adsorbed on $Zn_xCd_{1-x}S$ is further oxidized to form CO_3^{2-}. At the same time, CO_2 passes through $CO_2 \rightarrow {}^*CO_2 \rightarrow {}^*COOH \rightarrow {}^*CO \rightarrow CO$ pathway for CO production, and protons extracted from H_2O and PET are reduced to H_2 by collaboration with electrons, resulting in the formation of the tunable syngas H_2/CO.
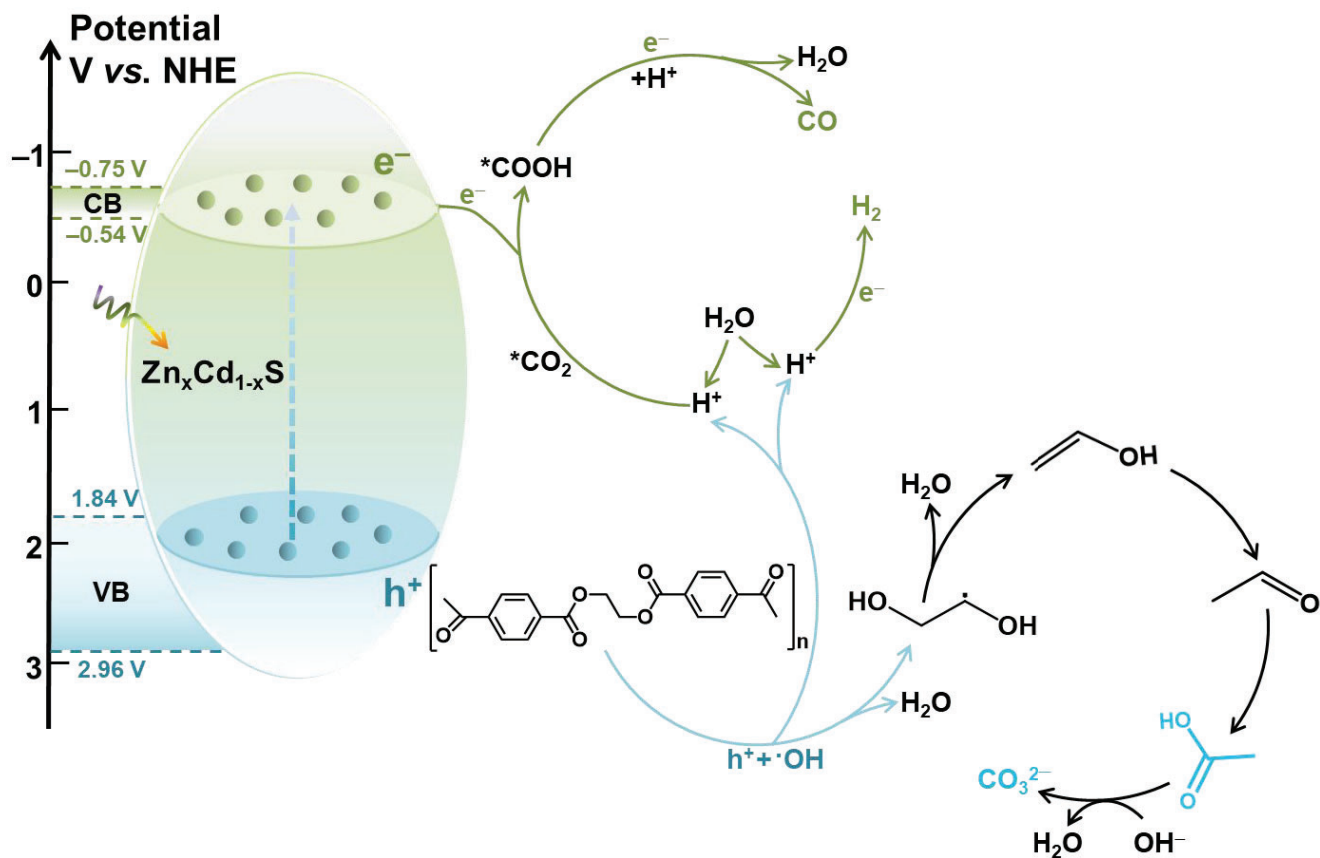
Figure 4. Proposed mechanism for the co-upcycling of CO_2 and PET into syngas and acetate catalyzed by $Zn_xCd_{1-x}S$.

In summary, we have demonstrated an effective heterogeneous photoredox-catalyzed system for the co-upcycling of CO_2 and PET into syngas and acetate catalyzed by $Zn_xCd_{1-x}S$ with a tunable band structure. The band structure of $Zn_xCd_{1-x}S$ photocatalysts is flexibly modulated by altering the Zn/Cd ratio, which results in the syngas H_2/CO production in a wide range. In addition, variations in the molar ratio of Zn/Cd also regulate the electron-hole separation ability, endowing $Zn_{0.8}Cd_{0.2}S$ with a highly effective charge carrier separation and transfer rate, thus exhibiting the excellent production rate of syngas and acetate. It is anticipated that this work provides a robust and proficient strategy for the heterogeneous coupling photocatalysis of merging PET conversion with CO_2 reduction into tunable syngas and acetate in a single redox reaction system by solar energy.

Experimental Section

Synthesis of $Zn_xCd_{1-x}S$. Uniform $Zn_xCd_{1-x}S$ nanospheres were synthesized using the co-precipitation method.[31] Typically, a certain amount of $Cd(CH_3COO)_2·2H_2O$ and $Zn(CH_3COO)_2·2H_2O$ were mixed into 60 mL EG under constant magnetic stirring. After 2 h, then 0.15 g NH_2CSNH_2 and 0.3 g PVP (M_w = 58000) were added. After ultrasound and stirring for 20 min at room temperature, the obtained transparent solution was then placed in a 100 mL capacity Teflon-lined stainless steel autoclave and maintained at 150 °C for 24 h, promoting the growth of $Zn_xCd_{1-x}S$. After being cooled down, the precipitate was washed three times and dried under vacuum

for 6 h to obtain the final product. In addition, the x in $Zn_xCd_{1-x}S$ refers to the different molar ratios of Zn (x = 0, 0.2, 0.4, 0.5, 0.6, 0.8, and 1).

Photoactivity Tests. Photocatalytic CO_2 reduction integrated with PET conversion was undertaken in a double-walled quartz reactor equipped with a flow-through water device to maintain room temperature. Typically, 10 mg catalysts were added into a mixture of PET pretreatment solution (1 mL) and deionized (DI) water (9 mL). The obtained homogeneous suspending solution was purged with CO_2 gas for 30 min. Subsequently, the full spectrum irradiation was carried out for 4 h. In the control experiment, sacrificial agents CCl_4, Na_2S and ML were used at 0.1 mmol. The 300 W Xe-lamp (CEL-HXF300-T3, Beijing China Education Au-light Co., Ltd., China) was used as a light source, and the light power density is measured to be approximately 300 mW cm^{-2}. The gas production was quantified by a gas chromatograph (Shimadzu GC-8A 2014C). The liquid phase products were qualitatively analyzed by ^{1}H NMR spectroscopy (JNM-ECZ600R), in which maleic anhydride was used as the internal-standard. The conversion (%) is calculated as $(n_0 - n)/n_0 \times 100\%$, where n_0 and n denote the molar amount of EG originally and finally, respectively.

ASSOCIATED CONTENT

Supporting Information.

The Supporting Information is available free of charge at http://pubs.acs.org.

Additional experimental details, characterization (crystal structures, morphologies, and optical absorption properties) and photoactivity results of the obtained sample. Energy band structure of $Zn_xCd_{1-x}S$, photoelectrochemical measurements of various samples.

AUTHOR INFORMATION

Corresponding Author
  Zi-Rong Tang — College of Chemistry, State Key Laboratory of Photocatalysis on Energy and Environment, Fuzhou University, Fuzhou 350116, P. R. China; School of Materials and Energy, University of Electronic Science and Technology of China, Chengdu 611731, P. R. China; orcid.org/0000-0002-6564-3539; Email: zrtang@fzu.edu.cn; zrtang@uestc.edu.cn
  Yi-Jun Xu — College of Chemistry, State Key Laboratory of Photocatalysis on Energy and Environment, Fuzhou University, Fuzhou 350116, P. R. China; Institute of Fundamental and Frontier Sciences, University of Electronic Science and Technology of China, Chengdu 611731, P. R. China; orcid.org/0000-0002-2195-1695; Email: yjxu@fzu.edu.cn; yjxu@uestc.edu.cn; Homepage: http://xugroup.fzu.edu.cn

Authors
  Yi Zhang — College of Chemistry, State Key Laboratory of Photocatalysis on Energy and Environment, Fuzhou University, Fuzhou 350116, P. R. China
  Ming-Yu Qi — Institute of Fundamental and Frontier Sciences, University of Electronic Science and Technology of China, Chengdu 611731, P. R. China; orcid.org/0000-0003-3937-1987
  Marco Conte — School of Mathematical and Physical Sciences, University of Sheffield, Sheffield, S3 7HF, UK; orcid.org/0000-0002-1399-0344

Author Contributions

Z.-R.T. and Y.-J.X. proposed the research direction and supervised the project. Y.Z. designed and preformed the experiments. Y.Z., M.-Y.Q., Z.-R.T., and Y.-J.X. and wrote and revised the manuscript. M.C. provided helpful suggestions. All authors participated in discussion and reviewed the paper before submission.

Notes

The authors declare no competing financial interest.

REFERENCES

(1) Li, X.; Yu, J.; Jaroniec, M.; Chen, X. Cocatalysts for Selective Photoreduction of CO_2 into Solar Fuels. *Chem. Rev.* **2019,** *119*, 3962–4179.

(2) Lu, K.-Q.; Li, Y.-H.; Zhang, F.; Qi, M.-Y.; Chen, X.; Tang, Z.-R.; Yamada, Y. M. A.; Anpo, M.; Conte, M.; Xu, Y.-J. Rationally Designed Transition Metal Hydroxide Nanosheet Arrays on Graphene for Artificial CO_2 Reduction. *Nat. Commun.* **2020,** *11*, 5181.

(3) Wu, H. L.; Li, X. B.; Tung, C. H.; Wu, L. Z. Semiconductor Quantum Dots: an Emerging Candidate for CO_2 Photoreduction. *Adv. Mater.* **2019,** *31*, 1900709.

(4) Jiang, H.; Wang, L.; Yu, X.; Sun, L.; Li, J.; Yang, J.; Liu, Q. Precise Regulation of Built-in Electric Field over NH_2-MIL-125-Ti/WO_{3-x} S-Scheme Heterojunction for Achieving Simultaneous Formation of CO and H_2O_2 from CO_2 and H_2O. *Chem. Eng. J.* **2023,** *466*, 143129.

(5) Zhu, B.; Hong, X.; Tang, L.; Liu, Q.; Tang, H. Enhanced Photocatalytic CO_2 Reduction over 2D/1D $BiOBr_{0.5}Cl_{0.5}$/WO_3 S-Scheme Heterostructure. *Acta Phys.-Chim. Sin.* **2021,** *38*, 2111008.

(6) Chu, S.; Ou, P.; Ghamari, P.; Vanka, S.; Zhou, B.; Shih, I.; Song, J.; Mi, Z. Photoelectrochemical CO_2 Reduction into Syngas with the Metal/Oxide Interface. *J. Am. Chem. Soc.* **2018,** *140*, 7869–7877.

(7) Habisreutinger, S. N.; Schmidt-Mende, L.; Stolarczyk, J. K. Photocatalytic Reduction of CO_2 on TiO_2 and Other Semiconductors. *Angew. Chem., Int. Ed.* **2013,** *52*, 7372–7408.

(8) Vesborg, P. C. K.; Seger, B. Performance Limits of Photoelectrochemical CO_2 Reduction Based on Known Electrocatalysts and the Case for Two-Electron Reduction Products. *Chem. Mater.* **2016,** *28*, 8844–8850.

(9) Ma, M.; Huang, Z.; Doronkin, D. E.; Fa, W.; Rao, Z.; Zou, Y.; Wang, R.; Zhong, Y.; Cao, Y.; Zhang, R.; Zhou, Y. Ultrahigh Surface Density of Co-N_2C Single-Atom-Sites for Boosting Photocatalytic CO_2 Reduction to Methanol. *Appl. Catal., B* **2022,** *300*, 120695.

(10) Ma, M.; Huang, Z.; Li, L.; Zhang, W.; Guo, R.; Zhang, R.; Fa, W.; Han, C.; Cao, Y.; Yu, S.;

Zhou, Y. Modulating Photogenerated Electron Density of Pr Single-Atom Sites by Coordination Environment Engineering for Boosting Photoreduction of CO_2 to CH_3OH. *Appl. Catal., B* **2023,** *330*, 122626.

(11) Han, C.; Li, Y.-H.; Li, J.-Y.; Qi, M.-Y.; Tang, Z.-R.; Xu, Y.-J. Cooperative Syngas Production and C–N Bond Formation in One Photoredox Cycle. *Angew. Chem., Int. Ed.* **2021,** *60*, 7962–7970.

(12) Khodakov, A. Y.; Chu, W.; Fongarland, P. Advances in the Development of Novel Cobalt Fischer-Tropsch Catalysts for Synthesis of Long-Chain Hydrocarbons and Clean Fuels. *Chem. Rev.* **2007,** *107*, 1692–1744.

(13) Yuan, L.; Qi, M.-Y.; Tang, Z.-R.; Xu, Y.-J. Coupling Strategy for CO_2 Valorization Integrated with Organic Synthesis by Heterogeneous Photocatalysis. *Angew. Chem., Int. Ed.* **2021,** *60*, 21150–21172.

(14) Artz, J.; Müller, T. E.; Thenert, K.; Kleinekorte, J.; Meys, R.; Sternberg, A.; Bardow, A.; Leitner, W. Sustainable Conversion of Carbon Dioxide: an Integrated Review of Catalysis and Life Cycle Assessment. *Chem. Rev.* **2017,** *118*, 434–504.

(15) Bao, Y.; Du, S.; Shibata, K.; Guo, X.; Kamakura, Y.; Feng, Z.; Huang, Y.; Ishitani, O.; Maeda, K.; Zhang, F. Layered β-ZrNBr Nitro-Halide as Multifunctional Photocatalyst for Water Splitting and CO_2 Reduction. *Angew. Chem., Int. Ed.* **2022,** *62*, e202214273.

(16) Guo, Q.; Liang, F.; Li, X.-B.; Gao, Y.-J.; Huang, M.-Y.; Wang, Y.; Xia, S.-G.; Gao, X.-Y.; Gan, Q.-C.; Lin, Z.-S.; Tung, C.-H.; Wu, L.-Z. Efficient and Selective CO_2 Reduction Integrated with Organic Synthesis by Solar Energy. *Chem* **2019,** *5*, 2605–2616.

(17) Pan, Y.-X.; You, Y.; Xin, S.; Li, Y.; Fu, G.; Cui, Z.; Men, Y.-L.; Cao, F.-F.; Yu, S.-H.; Goodenough, J. B. Photocatalytic CO_2 Reduction by Carbon-Coated Indium-Oxide Nanobelts. *J. Am. Chem. Soc.* **2017,** *139*, 4123–4129.

(18) Guo, Z.; Cheng, S.; Cometto, C.; Anxolabéhère-Mallart, E.; Ng, S.-M.; Ko, C.-C.; Liu, G.; Chen, L.; Robert, M.; Lau, T.-C. Highly Efficient and Selective Photocatalytic CO_2 Reduction by Iron and Cobalt Quaterpyridine Complexes. *J. Am. Chem. Soc.* **2016,** *138*, 9413–9416.

(19) Cao, B.; Wan, S.; Wang, Y.; Guo, H.; Ou, M.; Zhong, Q. Highly-Efficient Visible-Light-Driven Photocatalytic H_2 Evolution Integrated with Microplastic Degradation over MXene/$Zn_xCd_{1-x}S$ Photocatalyst. *J. Colloid Interface Sci.* **2022,** *605*, 311–319.

(20) Zhang, Y.; Qi, M.-Y.; Tang, Z.-R.; Xu, Y.-J. Photoredox-Catalyzed Plastic Waste Conversion: Nonselective Degradation versus Selective Synthesis. *ACS Catal.* **2023,** *13*, 3575–3590.

(21) Jiao, X.; Zheng, K.; Chen, Q.; Li, X.; Li, Y.; Shao, W.; Xu, J.; Zhu, J.; Pan, Y.; Sun, Y.; Xie, Y. Photocatalytic Conversion of Waste Plastics into C_2 Fuels Under Simulated Natural Environment Conditions. *Angew. Chem., Int. Ed.* **2020,** *59*, 15497–15501.

(22) Zhang, S.; Li, M.; Zuo, Z.; Niu, Z. Recent Advances in Plastic Recycling and Upgrading under Mild Conditions. *Green Chem.* **2023,** *25*, 6949–6970.

(23) Yuan, X.; Wang, X.; Sarkar, B.; Ok, Y. S. The COVID-19 Pandemic Necessitates a Shift to a Plastic Circular Economy. *Nat. Rev. Earth Environ.* **2021,** *2*, 659–660.

(24) Li, M.; Zhang, S. Tandem Chemical Depolymerization and Photoreforming of Waste PET Plastic to High-Value-Added Chemicals. *ACS Catal.* **2024,** *14*, 2949–2958.

(25) Bhattacharjee, S.; Guo, C.; Lam, E.; Holstein, J. M.; Rangel Pereira, M.; Pichler, C. M.; Pornrungroj, C.; Rahaman, M.; Uekert, T.; Hollfelder, F.; Reisner, E. Chemoenzymatic Photoreforming: A Sustainable Approach for Solar Fuel Generation from Plastic Feedstocks. *J. Am. Chem. Soc.* **2023,** *145*, 20355–20364.

(26) Zhang, S.; Li, H.; Wang, L.; Liu, J.; Liang, G.; Davey, K.; Ran, J.; Qiao, S.-Z. Boosted Photoreforming of Plastic Waste via Defect-Rich NiPS$_3$ Nanosheets. *J. Am. Chem. Soc.* **2023,** *145*, 6410–6419.

(27) Uekert, T.; Kuehnel, M. F.; Wakerley, D. W.; Reisner, E. Plastic Waste as a Feedstock for Solar-Driven H$_2$ Generation. *Energy Environ. Sci.* **2018,** *11*, 2853–2857.

(28) Du, M.; Zhang, Y.; Kang, S.; Guo, X.; Ma, Y.; Xing, M.; Zhu, Y.; Chai, Y.; Qiu, B. Trash to Treasure: Photoreforming of Plastic Waste into Commodity Chemicals and Hydrogen over MoS$_2$-Tipped CdS Nanorods. *ACS Catal.* **2022,** *12*, 12823–12832.

(29) Li, J.-Y.; Li, Y.-H.; Qi, M.-Y.; Lin, Q.; Tang, Z.-R.; Xu, Y.-J. Selective Organic Transformations over Cadmium Sulfide-Based Photocatalysts. *ACS Catal.* **2020,** *10*, 6262–6280.

(30) Yin, X.-L.; Li, L.-L.; Jiang, W.-J.; Zhang, Y.; Zhang, X.; Wan, L.-J.; Hu, J.-S. MoS$_2$/CdS Nanosheets-on-Nanorod Heterostructure for Highly Efficient Photocatalytic H$_2$ Generation under Visible Light Irradiation. *ACS Appl. Mater. Interfaces* **2016,** *8*, 15258–15266.

(31) Tang, L.; Kuai, L.; Li, Y.; Li, H.; Zhou, Y.; Zou, Z. Zn$_x$Cd$_{1-x}$S Tunable Band Structure-Directing Photocatalytic Activity and Selectivity of Visible-Light Reduction of CO$_2$ into Liquid Solar Fuels. *Nanotechnology* **2018,** *29*, 064003.

(32) Cui, X.; Zheng, Y. F.; Yin, H. Y.; Song, X. C. Novel C$_3$N$_4$/Zn$_{1-x}$Cd$_x$S Heterostructures with Adjustment of the Band Gap and Their Visible Light Photocatalytic Properties. *Phys. Chem. Chem. Phys.* **2015,** *17*, 29354–29362.

(33) Li, Y.; Wan, S.; Lin, C.; Gao, Y.; Lu, Y.; Wang, L.; Zhang, K. Engineering of 2D/2D MoS$_2$/Cd$_x$Zn$_{1-x}$S Photocatalyst for Solar H$_2$ Evolution Coupled with Degradation of Plastic in Alkaline Solution. *Sol. RRL* **2020,** *5*, 2000427.

(34) Akopov, G.; Yeung, M. T.; Sobell, Z. C.; Turner, C. L.; Lin, C.-W.; Kaner, R. B. Superhard Mixed Transition Metal Dodecaborides. *Chem. Mater.* **2016,** *28*, 6605–6612.

(35) Li, Y.; Sun, B.; Lin, H.; Ruan, Q.; Geng, Y.; Liu, J.; Wang, H.; Yang, Y.; Wang, L.; Chiu Tam, K. Efficient Visible-Light Induced H$_2$ Evolution from T-Cd$_x$Zn$_{1-x}$S/Defective MoS$_2$ Nano-Hybrid with both Bulk Twinning Homojunctions and Interfacial Heterostructures. *Appl. Catal., B* **2020,** *267*, 118702.

(36) Li, L.; Guo, C.; Ning, J.; Zhong, Y.; Chen, D.; Hu, Y. Oxygen-Vacancy-Assisted Construction of FeOOH/CdS Heterostructure as an Efficient Bifunctional Photocatalyst for CO$_2$ Conversion and Water Oxidation. *Appl. Catal., B* **2021,** *293*, 120203.

(37) Li, Q.; Meng, H.; Zhou, P.; Zheng, Y.; Wang, J.; Yu, J.; Gong, J. Zn$_{1-x}$Cd$_x$S Solid Solutions with Controlled Bandgap and Enhanced Visible-Light Photocatalytic H$_2$-Production Activity. *ACS Catal.* **2013,** *3*, 882–889.

(38) Chen, Y.; Zhao, S.; Wang, X.; Peng, Q.; Lin, R.; Wang, Y.; Shen, R.; Cao, X.; Zhang, L.; Zhou, G.; Li, J.; Xia, A.; Li, Y. Synergetic Integration of Cu$_{1.94}$S-Zn$_x$Cd$_{1-x}$S Heteronanorods for Enhanced Visible-Light-Driven Photocatalytic Hydrogen Production. *J. Am. Chem. Soc.* **2016,** *138*, 4286–4289.

(39) Wu, X.; Yu, Y.; Liu, Y.; Xu, Y.; Liu, C.; Zhang, B. Synthesis of Hollow Cd$_x$Zn$_{1-x}$Se Nanoframes through the Selective Cation Exchange of Inorganic-Organic Hybrid ZnSe-Amine Nanoflakes with Cadmium Ions. *Angew. Chem., Int. Ed.* **2012,** *51*, 3211–3215.

(40) Li, J.-Y.; Tan, C.-L.; Qi, M.-Y.; Tang, Z.-R.; Xu, Y.-J. Exposed Zinc Sites on Hybrid ZnIn$_2$S$_4$@CdS Nanocages for Efficient Regioselective Photocatalytic Epoxide Alcoholysis. *Angew. Chem., Int. Ed.* **2023,** *62*, e202303054.

(41) Qi, M.-Y.; Conte, M.; Tang, Z.-R.; Xu, Y.-J. Engineering Semiconductor Quantum Dots for Selectivity Switch on High-Performance Heterogeneous Coupling Photosynthesis. *ACS Nano* **2022,** *16*, 17444–17453.

(42) Uekert, T.; Kasap, H.; Reisner, E. Photoreforming of Nonrecyclable Plastic Waste over a Carbon Nitride/Nickel Phosphide Catalyst. *J. Am. Chem. Soc.* **2019,** *141*, 15201–15210.

(43) Qi, M.-Y.; Xu, Y.-J. Efficient and Direct Functionalization of Allylic sp^3 C-H Bonds with Concomitant CO_2 Reduction. *Angew. Chem., Int. Ed.* **2023,** *62*, e202311731.

(44) Bao, J.; He, J.; Zhang, Y.; Yoneyama, Y.; Tsubaki, N. A Core/Shell Catalyst Produces a Spatially Confined Effect and Shape Selectivity in a Consecutive Reaction. *Angew. Chem., Int. Ed.* **2007,** *47*, 353–356.

(45) Li, M.; Zhang, S. Coupling Waste Plastic Upgrading and CO_2 Photoreduction to High-Value Chemicals by a Binuclear Re–Ru Heterogeneous Catalyst. *ACS Catal.* **2024,** *14*, 6717–6727.

(46) Liu, M.; Xia, Y.; Zhao, W.; Jiang, R.; Fu, X.; Zimmerle, B.; Tian, L.; Chen, X. Modulating Oxygen Vacancy Concentration on $Bi_4V_2O_{11}$ Nanorods for Synergistic Photo-Driven Plastic Waste Oxidation and CO_2 Reduction. *J. Mater. Chem. A* **2023,** *11*, 12770–12776.

(47) Qin, J.; Dou, Y.; Zhou, J.; Zhao, D.; Orlander, T.; Andersen, H. R.; Hélix-Nielsen, C.; Zhang, W. Encapsulation of Carbon-Nanodots into Metal-Organic Frameworks for Boosting Photocatalytic Upcycling of Polyvinyl Chloride Plastic. *Appl. Catal., B* **2024,** *341*, 123355.

(48) Tan, C.-L.; Qi, M.-Y.; Tang, Z.-R.; Xu, Y.-J. Isolated Single-Atom Cobalt in the $ZnIn_2S_4$ Monolayer with Exposed Zn Sites for CO_2 Photofixation. *ACS Catal.* **2023,** *13*, 8317–8329.

(49) Chen, Y.-H.; Qi, M.-Y.; Li, Y.-H.; Tang, Z.-R.; Wang, T.; Gong, J.; Xu, Y.-J. Activating Two-Dimensional $Ti_3C_2T_x$-MXene with Single-Atom Cobalt for Efficient CO_2 Photoreduction. *Cell Rep. Phys. Sci.* **2021,** *2*, 100371.

(50) Qi, M.-Y.; Conte, M.; Anpo, M.; Tang, Z.-R.; Xu, Y.-J. Cooperative Coupling of Oxidative Organic Synthesis and Hydrogen Production over Semiconductor-Based Photocatalysts. *Chem. Rev.* **2021,** *121*, 13051–13085.

(51) Li, S.-H.; Qi, M.-Y.; Fan, Y.-Y.; Yang, Y.; Anpo, M.; Yamada, Y. M. A.; Tang, Z.-R.; Xu, Y.-J. Modulating Photon Harvesting through Dynamic Non-Covalent Interactions for Enhanced Photochemical CO_2 Reduction. *Appl. Catal., B* **2021,** *292*, 120157.

(52) Wang, Y.; Shang, X.; Shen, J.; Zhang, Z.; Wang, D.; Lin, J.; Wu, J. C. S.; Fu, X.; Wang, X.; Li, C. Direct and Indirect Z-Scheme Heterostructure-Coupled Photosystem Enabling Cooperation of CO_2 Reduction and H_2O Oxidation. *Nat. Commun.* **2020,** *11*, 3043.

(53) Yue, X.; Cheng, L.; Li, F.; Fan, J.; Xiang, Q. Highly Strained Bi-MOF on Bismuth Oxyhalide Support with Tailored Intermediate Adsorption/Desorption Capability for Robust CO_2 Photoreduction. *Angew. Chem., Int. Ed.* **2022,** *61*, e202208414.

(54) Shangguan, W.; Liu, Q.; Wang, Y.; Sun, N.; Liu, Y.; Zhao, R.; Li, Y.; Wang, C.; Zhao, J. Molecular-Level Insight into Photocatalytic CO_2 Reduction with H_2O over Au Nanoparticles by Interband Transitions. *Nat. Commun.* **2022,** *13*, 3894.

(55) Xin, Z. K.; Huang, M. Y.; Wang, Y.; Gao, Y. J.; Guo, Q.; Li, X. B.; Tung, C. H.; Wu, L. Z. Reductive Carbon–Carbon Coupling on Metal Sites Regulates Photocatalytic CO_2 Reduction in Water Using ZnSe Quantum Dots. *Angew. Chem., Int. Ed.* **2022,** *61*, e202207222.

(56) Sohlberg, K.; Leary, S. P.; Owen, N. L.; Trofimov, B. A. The Infrared Spectrum and Conformation of Acetone Oxime Vinyl Ether. *Vib. Spectrosc.* **1997,** *13*, 227–234.

(57) Melosso, M.; McGuire, B. A.; Tamassia, F.; Degli Esposti, C.; Dore, L. Astronomical Search of

Vinyl Alcohol Assisted by Submillimeter Spectroscopy. *ACS Earth Space Chem.* **2019,** *3*, 1189–1195.

(58) Kraeutler, B.; Bard, A. J. Heterogeneous Photocatalytic Decomposition of Saturated Carboxylic Acids on TiO_2 Powder. Decarboxylative Route to Alkanes. *J. Am. Chem. Soc.* **1978,** *100*, 19.